IOP Publishing | London Mathematical Society Nonlinearity

Nonlinearity **35** (2022) 1500–1520 https://doi.org/10.1088/1361-6544/ac4d91

Microscopic patterns in the 2D phase-field-crystal model

Gabriel Martine-La Boissonière, Rustum Choksi* and Jean-Philippe Lessard

Department of Mathematics and Statistics, McGill University, Montréal, QC, Canada

E-mail: gabriel.martine-laboissoniere@mail.mcgill.ca, rustum.choksi@mcgill.ca and jp.lessard@mcgill.ca

Received 2 February 2021, revised 17 January 2022
Accepted for publication 21 January 2022
Published 17 February 2022

Abstract

Using the recently developed theory of rigorously validated numerics, we address the phase-field-crystal model at the microscopic (atomistic) level. We show the existence of critical points and local minimizers associated with 'classical' candidates, grain boundaries, and localized patterns. We further address the dynamical relationships between the observed patterns for fixed parameters and across parameter space, then formulate several conjectures on the dynamical connections (or orbits) between steady states.

Keywords: phase field crystal, rigorously supported numerics, radial polynomial, grain boundary, polycrystalline materials

Mathematics Subject Classification numbers: 65P40.

S Supplementary material for this article is available online

(Some figures may appear in colour only in the online journal)

1. Introduction

The phase-field-crystal (PFC) model introduced in [1] is a gradient system capable of modelling a variety of solid-state phenomena. In its simplest form, the PFC energy can be written as

$$E[\psi] = \int_\Omega \frac{1}{2}\left(\nabla^2\psi + \psi\right)^2 + \frac{1}{4}\left(\psi^2 - \beta\right)^2$$

*Author to whom any correspondence should be addressed.
Recommended by Dr Claude Le Bris.

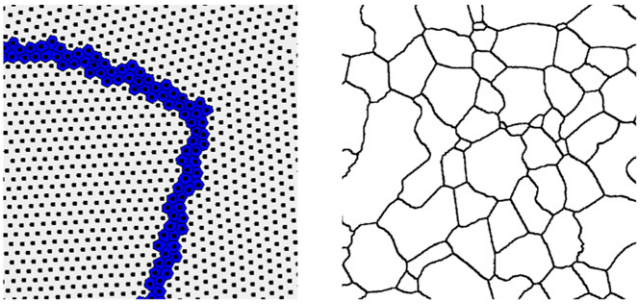

Figure 1. Left: details of a grain boundary appearing in a PFC simulation (taken from [3]). Right: grain boundary network from a PFC simulation (taken from [4]). Within each grain is a hexagonal lattice of atoms with a particular orientation.

defined on phase-fields $\psi \in H^2(\Omega)$ satisfying the *phase constraint*

$$\bar{\psi} = \fint_\Omega \psi = \frac{1}{|\Omega|}\int_\Omega \psi.$$

The parameter β represents inverse temperature such that $\beta = 0$ models maximum disorder. Coupled with this energy is its conservative H^{-1} gradient flow which entails the sixth-order partial differential equation (PDE) known as the PFC equation

$$\psi_t = \nabla^2\left(\left(\nabla^2 + 1\right)^2\psi + \psi^3 - \beta\psi\right).$$

Note that the PFC model shares its energy with the Swift–Hohenberg equation [2], which is simply the L^2 gradient flow of E. From linear stability analysis applied to single Fourier mode ansatz, we find three main candidate global minimizers that divide parameter space, see the supplementary material (https://stacks.iop.org/Non/35/031500/mmedia). In the hexagonal lattice regime, 2D-simulations of the PDE starting with random noise quickly produce atoms that arrange into small patches of hexagonal lattices with random orientations. These patches grow and interact with each other, forming *grains* of hexagonal lattices of atoms with a particular orientation. The morphology and evolution of these grains have features resembling those in polycrystalline materials (cf figure 1). In particular, it has recently been shown that statistics of many of experimentally observed (universal) grain boundary distributions are accurately captured by data amassed from simulations of this simple PFC equation [4, 5]. While here we will mostly work with this vanilla PFC formulation, we note that a family of PFC-like equations can be derived from density-functional-theory [6, 7] to obtain more complicated models capable of simulating eutectic and dendritic solidification [8] and graphene structures [9, 10]. There has also been work connecting PFC models with quasicrystals [11–13].

In this article, we address the PFC model and its steady states at the 'microscopic' level—the local atomic arrangement. We believe that such an investigation of microscopic pattern-formation capabilities of PFC is not only of mathematical interest but is also necessary to construct 'designer' models for polycrystalline behaviour. For example, varying the parameters in the energy lead to more complicated states than simple lamellar and hexagonal. These include localized patterns in the 'glassy regime'—the states near the liquid and solid transition—and 'globules' at large β.

With the exception of the constant (liquid) state (cf [14]), it is difficult to prove any theorem on the exact nature of steady states, local and global minimizers to this diffuse interface problem. What exists in the physics literature is numerical simulations, standard linear stability analysis, and ansatz-driven energy comparisons. The recently developed theory of rigorously validated numerics (cf [15–19]) now provides a powerful new tool to bridge what can be observed numerically with rigorous statements on pattern morphology. In a nutshell this approach can be summarized as follows: given an approximate steady state, we use the *contraction mapping theorem* to imply the existence and local uniqueness of an *exact* steady state within a *controlled distance* of the approximation. This notion of closeness is strong enough to imply further useful results, including closeness in energy and stability results. In this paper we use this new approach to address the following aspects of the PFC model:

- Are the 'classical' candidates obtained from linear stability analysis close to actual local minimizers?
- Are the stable yet complicated patterns observed numerically indeed critical points in the PFC energy landscape? For example, are grain boundaries steady states or simply metastable states?
- What are the *dynamical* relationships between the observed patterns for fixed parameters and across parameter space?

Based upon our results we formulate several conjectures on the connections (or orbits) between steady states. Taken as a whole, our work presents the first step into a rigorous analysis of the rich PFC energy landscape.

The outline of this paper is as follows. We first setup the PFC equation in Fourier space and discuss the application of the framework of rigorous computations. We then verify the existence of important steady states of the PFC equation, including localized patterns and grain boundaries. With these states in hand, we address the *energy landscape* of PFC with a discussion on conjectures for connections (or connecting orbits) between steady states. Finally, we presents results in one-parameter numerical continuation to outline some interesting features of the bifurcation diagram of PFC.

2. PFC steady states in Fourier space

We begin by writing the equation $\psi_t = 0$ in Fourier space to obtain a coupled system of equations for the Fourier coefficients of steady states. We will be slightly more general and consider functionals of the form

$$E[\psi] = \fint_\Omega \frac{1}{2}(K\psi)^2 + \frac{1}{4}(\psi^2 - \beta)^2,$$

where K is a linear differential operator acting on elements of a suitable function space. In particular,

$$K = \begin{cases} \nabla^2 + 1 & \text{for the basic 'one} - \text{mode' PFC model} \\ (\nabla^2 + 1)(\nabla^2 + q^2) & \text{for the 'two} - \text{mode' PFC model [20]} \end{cases},$$

where q is the secondary wavelength of two-mode PFC. Taking the H^{-1} gradient flow of E, we obtain the PFC-like equation $\psi_t = \nabla^2\left(\left(K^2-\beta\right)\psi+\psi^3\right)$.

For simplicity, we let Ω be the rectangular domain $[0, L_x]\times[0, L_y]$ with periodic boundary conditions. We let

$$L_x = \frac{4\pi}{\sqrt{3}}N_x \qquad L_y = 4\pi N_y,$$

where $N_x, N_y \in \mathbb{N}$ are the number of atoms lined up in the x, y-axes. The main parameters of the problem are then $(\bar{\psi}, \beta)$ and the domain size is given by (N_x, N_y).

Let a_α be the Fourier coefficients of ψ and let $(a_\alpha)_t$ be the time derivative. Inserting this expansion into the PFC equation results in an infinite system of equations of the form $(a_\alpha)_t = F_\alpha(a)$ thanks to orthogonality. The steady states may then be found numerically by solving $F(a) = 0$ up to some truncation order M. We will see later that it is imperative to isolate the zeros of F; the *continuous* translational and rotational symmetries of PFC must then be broken. The simplest way to do so in this context is to also enforce Neumann boundary conditions. It is convenient to write $a_\alpha = a_{\alpha_1,\alpha_2}$ so that the symmetry and reality conditions become $a_{|\alpha_1|,|\alpha_2|}\in\mathbb{R}$.

This choice allows us to simplify a complex Fourier series into the cosine expansion

$$\begin{aligned}\psi(x,y) &= \sum_{\alpha\in\mathbb{Z}^2} a_\alpha \exp\left(2\pi \mathrm{i}\frac{\alpha_1 x}{L_x}\right)\exp\left(2\pi\mathrm{i}\frac{\alpha_2 y}{L_y}\right)\\ &= \sum_{\alpha\in\mathbb{N}^2} W_\alpha a_\alpha \cos\left(\frac{2\pi\alpha_1}{L_x}x\right)\cos\left(\frac{2\pi\alpha_2}{L_y}y\right),\end{aligned}$$

where W is a *weight matrix* defined by

$$W_\alpha = \begin{cases} 1 & \text{if } \alpha = (0,0)\\ 2 & \text{if } \alpha_1 = 0, \alpha_2 \neq 0 \text{ or } \alpha_1 \neq 0, \alpha_2 = 0\\ 4 & \text{otherwise.}\end{cases}$$

The Fourier coefficients of $\nabla^2\psi$ are given by the elementwise product $L_\alpha a_\alpha$ where

$$L_\alpha = -\left(\left(\frac{2\pi\alpha_1}{L_x}\right)^2 + \left(\frac{2\pi\alpha_2}{L_y}\right)^2\right)$$

is the Fourier representation of the Laplacian. Inserting these expressions into the PFC equation and equating Fourier modes, we obtain

$$(a_\alpha)_t = F_\alpha(a) = L_\alpha\left(\gamma_\alpha a_\alpha + (a*a*a)_\alpha\right),$$

where $*$ denotes the discrete convolution and the linear terms combining K and β are

$$\gamma_\alpha = \begin{cases} (L_\alpha+1)^2-\beta & \text{for PFC}\\ (L_\alpha+1)^2\left(L_\alpha+q^2\right)^2-\beta & \text{for two}-\text{mode PFC.}\end{cases}$$

Note that the $(0,0)$ Fourier component picks out the average phase so it is fixed to $\bar{\psi}$: this is consistent with $(a_{0,0})_t = 0$ thanks to $L_{0,0} = 0$. To keep track of the phase constraint directly in F, we replace its first trivial component by $F_{0,0} = a_{0,0} - \bar{\psi}$, resulting in:

$$F_\alpha(a) = \begin{cases} a_{0,0} - \bar{\psi} & \text{if } \alpha = (0,0) \\ L_\alpha\left(\gamma_\alpha a_\alpha + (a * a * a)_\alpha\right) & \text{otherwise.} \end{cases}$$

The operator F then represents the PFC dynamics in the sense that its zeros correspond to steady states of the PFC equation. A numerical advantage of the reduced expansion is that we effectively only have to compute a quarter of the full Fourier series. Obviously, this means we are not treating PFC in full generality over H^2 and will have to address this later. As an aside, the equivalent F for Swift–Hohenberg is simply $-(\gamma_\alpha a_\alpha + (a * a * a)_\alpha)$ hence its $(0,0)$ entry is nonzero and average phase is not conserved.

3. Overview of rigorously validated numerics and application of the radii polynomial approach for PFC

As we just mentioned, our main tool for addressing the steady states of the PFC functional is the radii polynomial approach for rigorously validated numerics. The purpose of this section (and material presented in the supplementary material) is to provide sufficient detail so that the reader can appreciate and indeed verify our results. From the point of view of the theory there is nothing new here; nevertheless, leaving out the details would leave the uninitiated reader without the tools to evaluate and assess our results.

The recent framework of rigorous computations has significantly enhanced the study of dynamical systems. Examples of early pioneering works in the field of rigorous computations is the proof of the universality of the Feigenbaum constant [21] and the proof of existence of the strange attractor in the Lorenz system [22]. Several computer-assisted proofs of existence of solutions to PDEs have also been presented in the last decades including eigenvalues enclosure methods [23], self-consistent *a priori* bounds [24, 25], *a priori* error estimates for finite element approximations combined with the Schauder fixed point theorem [26, 27] and topological methods based on Conley index theory [28, 29]. We refer the interested reader to the survey papers [15–19], as well as the recent book [30]. In the present paper, our computer-assisted proofs are based on combining a standard Newton–Kantorovich approach with the contraction mapping theorem, which is an idea that has been developed by several authors and which is at the center of a well-developed literature (e.g. see [31–37] for some early work). We briefly review the fundamentals of our approach and refer to [38] for more details.

Consider the Newton operator $T(a) = a - AF(a)$, where A is a suitable inverse to the derivative $DF(a)$. On one hand, if T is a contraction on a closed ball, the Banach fixed-point theorem gives the existence and uniqueness of a zero of F within this ball. On the other, the repeated application of T (allowing A to vary with a) should converge to this fixed point. We can then *numerically* compute an approximate steady state $\bar{a}$ for which $F(\bar{a}) \approx 0$ up to numerical precision. If in addition we are able to show that T is a contraction around $\bar{a}$, then we immediately have the existence of an exact steady state $\widetilde{a}$ close to $\bar{a}$ in an appropriate metric. This relationship is made clear by the *radii polynomial theorem*, so-called for reasons that will become clear shortly. To illustrate the method, we specialize the theorem to the case applicable to PFC, but see [39, 40] for an applications to Ohta–Kawasaki in 2D and 3D. Given Banach spaces X, Y, we

use the notation $B(X, Y)$ for the space of bounded linear operators from X to Y, $B(X) = B(X, X)$ and $B_r(a) \subset X$ for the open ball of radius r around $a \in X$.

Theorem 1. *Consider Banach spaces X, Y, a point $\bar{a} \in X$ and let $A^\dagger \in B(X, Y)$, $A \in B(Y, X)$. Suppose $F : X \to Y$ is Fréchet differentiable on X and A is injective. In addition, suppose*

$$\begin{aligned} \|AF(\bar{a})\|_X &\leqslant Y_0 \\ \|I - AA^\dagger\|_{B(X)} &\leqslant Z_0 \\ \|A(DF(\bar{a}) - A^\dagger)\|_{B(X)} &\leqslant Z_1 \\ \|A(DF(b) - DF(\bar{a}))\|_{B(X)} &\leqslant Z_2(r)r \quad \forall\, b \in \overline{B_r(\bar{a})} \end{aligned}$$

where Y_0, Z_0, Z_1 are positive constants and Z_2 is a positive polynomial in $r > 0$. Construct the radii polynomial

$$p(r) = Z_2(r)r^2 - (1 - Z_0 - Z_1)r + Y_0. \tag{1}$$

If $p(r_0) < 0$ for some $r_0 > 0$, then there exists a unique $\widetilde{a} \in B_{r_0}(\bar{a})$ for which $F(\widetilde{a}) = 0$.

For completeness, the proof of this formulation is given in supplementary material section 2, where we show a correspondence between the sign of the radii polynomial and the contraction constant of T: if r_0 can be found, T is a contraction and the Newton iteration starting at $\bar{a}$ must converge to some $\widetilde{a}$. This proves not only the existence of the exact steady states but also gives control on its location in X with respect to a known point. In practice, one finds an interval $[r_*, r^*]$ of radii for which $p(r)$ is negative; $r_* > 0$ gives the *maximum* distance between $\bar{a}$ and $\widetilde{a}$ while $r^* > r_*$ gives the *minimum* distance between $\bar{a}$ and *another* zero of F. The zeros of F must therefore be isolated for consistency.

Each bound may be understood intuitively: Y_0 being small indicates that $\bar{a}$ is a good approximation of $\widetilde{a}$ while Z_1 being small indicates that $A^\dagger$ is a good approximation for $DF(\bar{a})$, and so on. These bounds may be simplified analytically but must necessarily be computed numerically. Therefore, we ensure that our numerical computations go in the same direction as the required inequalities by using interval arithmetic [41], a formalized approach to deal with numerical errors. We used the interval arithmetic package INTLAB for MATLAB, see [42, 43], to ensure that the radii polynomial approach is numerically rigorous.

This approach can be applied to the PFC equation to prepare numerical tools that can both find a candidate steady state and compute the radii r_*, r^* if they exist. If so, we immediately have a *proof* that this candidate provides a good handle on an actual state of the PFC equation. To do so, the derivative DF is computed and the underlying Banach space is specialized as follows.

Let $\nu > 1$ and define $\ell^1_\nu(\mathbb{Z}^2)$ as the space of sequences a_α with finite norm

$$\|a\|_{1,\nu} = \sum_{\alpha \in \mathbb{Z}^2} |a_\alpha| \nu^{|\alpha|} = \sum_{\alpha \in \mathbb{Z}^2} |a_\alpha| \nu^{|\alpha_1| + |\alpha_2|}.$$

The restriction of $\ell^1_\nu(\mathbb{Z}^2)$ using the symmetry condition is

$$X = \left\{ a \in \ell^1_\nu(\mathbb{Z}^2) \,\middle|\, a_\alpha = a_{|\alpha_1|, |\alpha_2|} \right\}$$

over which the norm simplifies to

$$\|a\|_{1,\nu} = \sum_{\alpha\in\mathbb{N}^2} W_\alpha |a_\alpha| \nu^{|\alpha|} = \sum_{\alpha\in\mathbb{N}^2} |a_\alpha| \nu_\alpha$$

where ν_α is a weight matrix that forces the fast exponential decay of the Fourier coefficients. The space $(X, \|\cdot\|_{1,\nu})$ can easily be shown to be Banach and the 2D discrete convolution forms a Banach algebra over it, immediate results from the triangle inequality and the fact that $\nu > 1$.

To implement Newton's method numerically and obtain a numerical approximation $\bar{a}$, we consider a finite dimensional projection of F. Given a truncation order M, denote by $a^{(M)}, F^{(M)}$ the $(M+1)^2$ matrices consisting of keeping only the Fourier modes of order at most M in a and F, respectively. For instance, $a^{(M)}$ is obtained by setting $a_\sigma = 0$ whenever *either* σ_1 or σ_2 is greater than M.

Let now $\bar{a}, \widetilde{a} \in X$ have the same meaning as before, with $\bar{a} = 0$ outside of $U = \{0, 1, \ldots, M\}^2$ thanks to the truncation. Let $G = DF(\bar{a})^{(M)}$ and denote by $A^{(M)}$ the numerical inverse of G. We define *approximate* operators $A^\dagger, A$ as

$$A^\dagger_{\alpha,\sigma} = \begin{cases} G_{\alpha,\sigma} & \text{if } \alpha,\sigma \in U \\ L_\alpha \gamma_\alpha & \text{if } \alpha = \sigma, \alpha \in \mathbb{N}^2 \backslash U \\ 0 & \text{otherwise,} \end{cases} \qquad A_{\alpha,\sigma} = \begin{cases} A^{(M)}_{\alpha,\sigma} & \text{if } \alpha,\sigma \in U \\ L_\alpha^{-1}\gamma_\alpha^{-1} & \text{if } \alpha = \sigma, \alpha \in \mathbb{N}^2 \backslash U \\ 0 & \text{otherwise} \end{cases}$$

which can be thought of as block tensors containing G or its inverse paired with the *linear terms* $L_\alpha\gamma_\alpha$ as the *main 'diagonal'* of the second block. If G is an invertible matrix[1], so is A and it is thus injective. The inverse of A is *not* $A^\dagger$ however because $A^{(M)}G \approx I^{(M)}$ only up to numerical inversion errors.

Note that F, DF and $A^\dagger$ map to a space Y with less regularity than X because of the unbounded $L_\alpha\gamma_\alpha$ terms arising from *real space derivatives*; Y is a space where sequences $L_\alpha\gamma_\alpha a_\alpha$ have finite norm. However, the operator products against A *are* bounded on X thanks to the *fast* decay of $L_\alpha^{-1}\gamma_\alpha^{-1}$. Thus, we say that A 'lifts' the regularity of the other operators back to X, allowing statements such as $T : X \to X$ or $ADF(\bar{a}) \in B(X)$.

We show in supplementary material section 3 how to simplify the bounds into expressions that can be evaluated numerically. This allows us to write down the radii polynomial $p(r) = Z_2(r)r^2 - (1 - Z_0 - Z_1)r + Y_0$, noting that $Z_2(r) = Z_2^{(0)} + Z_2^{(1)}r$, hence the polynomial is cubic with non-negative coefficients except for maybe the linear term. We have $p(0) > 0$, $p'(0) = Z_0 + Z_1 - 1$ and $p(r) \to \infty$ for large r. As a consequence, if p is strictly negative for some positive r, there must exist exactly two strictly positive roots $r_* < r^*$ defining the interval where the proof is applicable. When this is satisfied, the radii polynomial theorem gives that

(a) There exists an exact solution $\widetilde{a}$ of $F(a) = 0$ in $B_{r_*}(\bar{a})$.
(b) This solution is unique in $\overline{B_{r^*}(\bar{a})}$.

Thus, when the radii polynomial is computed using interval arithmetic and has exactly two real non-negative roots, the zero computed numerically with the Newton iteration is close to an actual steady state of the PFC equation. Note the important fact that the ball is in X so *a priori*, only the Fourier coefficients are controlled. Thanks to $\nu > 1$ however, we show in

[1] The numerical method will fail if G is almost singular, so this is the case in practice.

supplementary material section 4 that this control translates into closeness in energy and in real space norms. In particular, the distance *in value* between the phase fields corresponding to $\bar{a}$ and $\widetilde{a}$ is at most r_*.

Further, we show in supplementary material section 5 that the stability of $\widetilde{a}$ in X is controlled by the eigenvalues of G. It is important to observe that this matrix will always have a positive eigenvalue because of the trivial condition $F_{0,0} = a_{0,0} - \bar{\psi}$. This is *not* indicative of instability in the context of the H^{-1} gradient flow because $a_{0,0}$ is fixed. We shall see later that this unstable direction can be used to compute a *branch of solutions* in parameter continuation. For now however, we call the number of positive eigenvalues, minus 1, the *Morse index* of $\widetilde{a}$, indicating how many unstable directions are available to a given steady state for *fixed* parameters.

The procedure to numerically investigate the steady states of the PFC equation is as follows:

- Starting from a given initial condition, the Newton iteration is run until it converges up to numerical precision.
- Then, the radii polynomial of the numerical guess is computed and its roots are tested.
- If the proof succeeds, we can characterize an exact steady state in value, in energy and compute its stability in X. The parameters (M, ν) can be adjusted until the proof succeeds with a trade-off between the computational effort and closeness in X.

In order for the reader to verify the success of the method for the presented states (patterns), we have provided the coefficient data and processing algorithms at the following site: https://github.com/gmartinemath/pfc-steady-states.

4. Rigorous results on small domains

We now have a complete framework for finding verified steady states along with their energetic and stability properties. This allows us to understand the behaviour of the PFC system for a given choice of $(\bar{\psi}, \beta)$, with three important caveats:

- We cannot guarantee that we have found *all* steady states and therefore *the* global minimizer. Indeed, we may only hope to cover a reasonable portion of the underlying space by sampling initial conditions randomly.
- The size of M must be balanced with ν to keep r_* as small as possible, keeping in mind that r^* is ultimately bounded above by the distance between two steady states. In particular, large domains and large β increase the contribution of high frequency Fourier modes, hence the truncation order can become large even for domains containing only 100 atoms. This limits our results to small domains so our analysis is 'small scale' in nature.
- The Neumann boundary conditions restrict us to a 'quadrant' of H^2. While the existence of a steady state, the energy bound and *instability* obviously extend to H^2, stability *does not* as there may be unstable directions in the other three Fourier series that are missed by the current method.

For the last point, we sometimes observe that translational shifts have a different Morse index in X. This is observed for example with the stripes states, see figure 3(a). In this sense, we only provide a *lower bound* for Morse indices in H^2.

Table 1. Data for selected values of $(\bar{\psi}, \beta)$ on the exact steady states $\widetilde{a}$ near the numerical approximation $\bar{a}$, obtained from the original candidate a. $M = 20, 30, 40$ for each parameter set respectively. The Morse index was verified in X. We write $<\epsilon$ when the number was numerically computed as 0. E_0 denotes the energy of the constant state.

Ansatz	$(\bar{\psi}, \beta)$	$\|\bar{a}\|_{1,\nu}$ $\|a - \bar{a}\|_{1,\nu}$	r_* r^*	$E[\bar{a}] - E_0$ $\|E[\bar{a}] - E[\widetilde{a}]\|$	Morse index
	$(0.07, 0.025)$	0.07 $<\epsilon$	4.3×10^{-16} 1.7×10^{-2}	4.337×10^{-19} 4.9×10^{-17}	4
	$(0.3, 0.5)$	0.30 $<\epsilon$	1.1×10^{-14} 1.9×10^{-2}	1.388×10^{-17} 1.5×10^{-14}	16
	$(0.5, 1.0)$	0.50 $<\epsilon$	7.2×10^{-15} 5.3×10^{-3}	$<\epsilon$ 2.6×10^{-14}	16
	$(0.07, 0.025)$	0.21 4.8×10^{-4}	7.3×10^{-13} 5.7×10^{-3}	-1.774×10^{-5} 4.8×10^{-13}	0
	$(0.3, 0.5)$	1.02 4.5×10^{-2}	1.9×10^{-11} 1.2×10^{-3}	-9.369×10^{-3} 8.3×10^{-11}	7
	$(0.5, 1.0)$	1.31 1.1×10^{-1}	1.2×10^{-12} 1.7×10^{-2}	-1.241×10^{-2} 9.1×10^{-12}	11
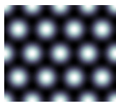	$(0.07, 0.025)$	0.41 1.1×10^{-3}	1.0×10^{-11} 6.8×10^{-3}	-4.714×10^{-5} 1.5×10^{-11}	0
	$(0.3, 0.5)$	1.92 8.1×10^{-2}	5.5×10^{-10} 4.5×10^{-3}	-2.089×10^{-2} 8.1×10^{-9}	0
	$(0.5, 1.0)$	2.79 2.4×10^{-1}	1.3×10^{-11} 2.9×10^{-3}	-5.897×10^{-2} 4.4×10^{-10}	0
	$(0.07, 0.025)$	0.19 7.6×10^{-4}	1.4×10^{-13} 3.2×10^{-3}	-3.013×10^{-6} 8.1×10^{-14}	3
	$(0.3, 0.5)$	0.99 8.8×10^{-2}	3.7×10^{-12} 2.9×10^{-3}	-1.839×10^{-3} 1.6×10^{-11}	12
	$(0.5, 1.0)$	1.09 1.0×10^{-1}	4.7×10^{-12} 2.1×10^{-3}	-1.312×10^{-3} 2.1×10^{-11}	16

4.1. Verification of the candidate minimizers

The candidate global minimizers (constant, stripes, atoms and donuts states) introduced in supplementary material section 1 have trivial Fourier coefficients by construction, given by

$$\begin{aligned} \text{Constant: } & a_{0,0} = \bar{\psi} \\ \text{Stripes: } & a_{0,0} = \bar{\psi} \qquad a_{0,2N_y} = \frac{1}{2}A_s \\ \text{Hexagonal: } & a_{0,0} = \bar{\psi} \qquad a_{N_x,N_y} = \frac{1}{2}A_h \quad a_{0,2N_y} = \frac{1}{2}A_h \end{aligned} \quad ,$$

where A_s, A_h represent amplitudes that optimize the PFC energy calculation. Note that A_h differs between the atoms and donuts states.

Table 2. Data on steady states for $(\bar{\psi}, \beta) = (0.07, 0.025)$ and $(N_x, N_y) = (8, 5)$, capturing roughly 80 atoms. The observed count is the number of times the steady state, including its discrete translational shifts, were reached out of 200 randomized trials.

Visualization	r_* r^*	$E[\bar{a}] - E_0$ $\lvert E[\bar{a}] - E[\widetilde{a}]\rvert$	Morse index	Count
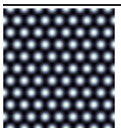	1.0×10^{-8}	-4.714×10^{-5}		
			0	53
	2.8×10^{-3}	2.2×10^{-8}		
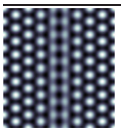	2.5×10^{-8}	-2.358×10^{-5}		
			0	21
	2.9×10^{-4}	6.7×10^{-8}		
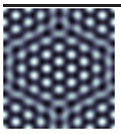	5.4×10^{-8}	-2.215×10^{-5}		
			0	57
	5.8×10^{-5}	1.9×10^{-7}		
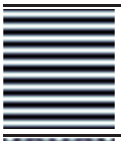	1.6×10^{-9}	-1.774×10^{-5}		
			1	0
	2.0×10^{-3}	1.3×10^{-9}		
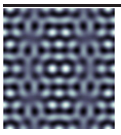	3.5×10^{-8}	-1.161×10^{-5}		
			2	1
	5.4×10^{-5}	9.0×10^{-8}		

To illustrate the approach, we first applied the verification program starting at the atoms state b constructed for $(\bar{\psi}, \beta) = (0.07, 0.025)$, $(N_x, N_y) = (4, 2)$ and $M = 20$. The Newton iteration was used to obtain $\bar{b}$ for which the radii polynomial was tested with $\nu = 1.05$, resulting in $r_* = 1.0 \times 10^{-11}$ and $r^* = 6.8 \times 10^{-3}$. The ℓ^1_ν distance between b and $\bar{b}$ is 1.1×10^{-3}, indeed smaller than r^*.

The difference $b - \bar{b}$ is mainly captured by *new* Fourier modes: we find that the main Fourier coefficients $b_{N_x,N_y} = b_{0,2N_y} = -4.4 \times 10^{-2}$ differ by 1.5×10^{-5} while the largest *new* Fourier modes are $b_{8,0} = b_{4,5} = -7.4 \times 10^{-5}$. Moreover, the distance in the (numerical) sup norm between the two *phase fields* is approximately 4.4×10^{-4} which is again smaller than the ℓ^1_ν distance, consistent with the L^∞ bound.

This approach was repeated for the other candidates and for a few other choices of the PFC parameters in the hexagonal regime, with truncation adjusted to β. The results are presented in table 1, showing that such simple candidates capture well the leading behaviour. Note that the agreement decreases with increasing β: compare the size of $\|a - \bar{a}\|_{1,\nu}$ to $\|\bar{a}\|_{1,\nu}$.

4.2. Steady states in the hexagonal lattice regime

The Newton iteration can detect new steady states regardless of stability as it is based on criticality instead of minimality. This allows us to find steady states that are observed only *momentarily* or even *locally* during a PFC simulation. Table 2 presents a few of the 28 distinct steady states found for $(\bar{\psi}, \beta) = (0.07, 0.025)$, $(N_x, N_y) = (8, 5)$, $\nu = 1.05$ and $M = 40$. Starting at random initial coefficient matrices, the Newton iteration converges in 15 to 50 steps.

Table 3. Data on steady states for $(\bar{\psi}, \beta) = (0.5, 0.6)$ and $(N_x, N_y) = (7, 4)$. No count is provided because only a few trials were attempted.

Visualization	r_* r^*	$E[\bar{a}] - E_0$ $\lvert E[\bar{a}] - E[\widetilde{a}]\rvert$	Morse index
	9.9×10^{-11} 3.3×10^{-4}	-2.465×10^{-3} 4.7×10^{-9}	0
	1.6×10^{-10} 2.4×10^{-4}	-1.457×10^{-3} 1.9×10^{-8}	1
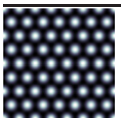	2.6×10^{-10} 7.7×10^{-5}	-2.670×10^{-4} 2.3×10^{-9}	8
	2.1×10^{-11} 1.3×10^{-3}	-6.420×10^{-5} 3.0×10^{-10}	0
	9.3×10^{-15} 4.8×10^{-2}	$<\epsilon$ 2.8×10^{-14}	0
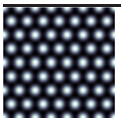	1.7×10^{-11} 1.6×10^{-3}	5.629×10^{-4} 5.7×10^{-11}	20

The four main ansatz were also explicitly tested, as only the atoms state could be reached from random initial conditions.

Note that the energy of the exact steady states can be compared from table 2: for instance, the energy of the *exact* atoms state is bounded away from the others so it is guaranteed to be the best candidate global minimizer out of the observed steady states at the current parameter values.

The second and third states presented in the table clearly display two grains of the same orientation but with boundary atoms meeting 'head-to-head'. This is essentially an intermediate in the grains slipping on one another that is stabilized by the restrictions of the boundary conditions. Such states then represent a grain boundary that is stable, at least in X. When PFC simulations [44] are initialized at these states, the flow appears to be stable for thousands of steps then suddenly goes to the hexagonal lattice, meaning there are unstable directions in the rest of H^2. Nevertheless, the fact remains that grain boundaries can be *steady states*.

Table 4. Data on steady states for $(\bar{\psi}, \beta) = (2.5, 20.0)$ and $(N_x, N_y) = (4, 2)$.

Visualization	r_* r^*	$E[\bar{a}] - E_0$ $\lvert E[\bar{a}] - E[\widetilde{a}]\rvert$	Morse index
	1.5×10^{-8} 5.0×10^{-5}	-36.71 5.8×10^{-4}	0
	1.2×10^{-9} 2.6×10^{-4}	-35.48 3.5×10^{-6}	0
	2.3×10^{-8} 2.9×10^{-5}	-35.08 1.0×10^{-3}	0
	1.2×10^{-7} 4.4×10^{-6}	-24.11 4.6×10^{-4}	13

4.3. Steady states in the localized patterns regime

Table 3 presents some steady states found for $(\bar{\psi}, \beta) = (0.5, 0.6)$, $(N_x, N_y) = (7, 4)$, $\nu = 1.01$ and $M = 60$. In this regime, localized or coexistence patterns are observed in PFC simulations, some of which we can confirm to be steady states: note in particular the existence of a 'single atom' state. We see here that the global minimizer cannot be of the four main ansatz. We observe *two* atoms states with different amplitudes and stability, highlighting the fact that the 'linear' candidate is no longer appropriate as β increases and nonlinear effects begin to dominate the energy.

Similar results have been obtained previously for a version of Swift–Hohenberg with broken $\psi \to -\psi$ symmetry, see [45, 46].

4.4. Steady states for the large β regime

Table 4 shows a selection of steady states found in the large β regime, $(\bar{\psi}, \beta) = (2.5, 20.0)$, $(N_x, N_y) = (4, 2)$, $\nu = 1.01$ and $M = 65$. In this regime, the microscopic organization is lost as constant patches of phase form, with value close to $\pm\sqrt{\beta}$, meaning that the double well term of the PFC functional dominates the oscillation term.

4.5. Phase diagram with verified steady states

The framework allows us to construct a 'rigorous' phase diagram for PFC. Here the adjective 'rigorous' does **not** mean that we have identified the ground state; but rather that the respective candidate state has been rigorously verified in its parameter regime. To this end, one must construct a 'patchwork' of $(\bar{\psi}, \beta)$ split in regions in which we have a proof that a given state is a global minimizer. For now, we restrict ourselves to proving that one of the steady states near the known candidate minimizers has lower energy than all other *known* steady states at given *points*. Further, our attempt is somewhat limited by the small domains we can access.

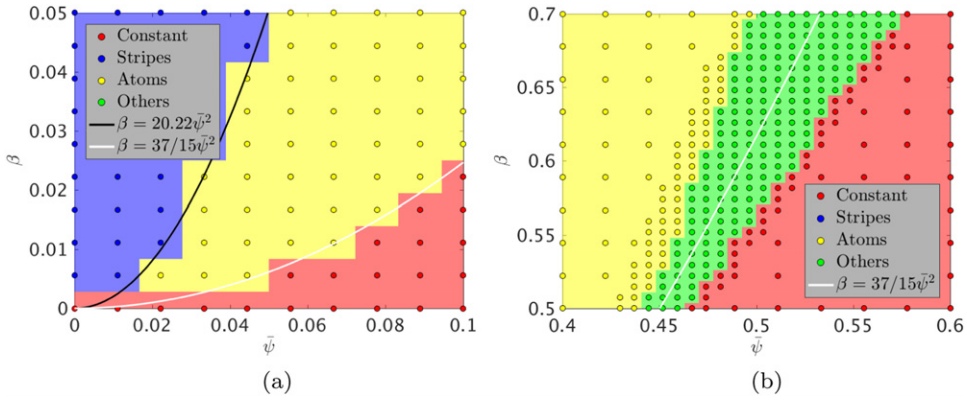

Figure 2. Phase diagram for small parameter values (a) and for the localized patterns regime. (b) All points are prepared by rigorously verifying that the exact steady state around the ansatz have lower energy than all other observed steady states, up to translational shifts. Coloured regions are filled in to guide the eye. The curves show the condition for the energy of the basic ansatz to be equal.

Nevertheless, this construction is useful and does indicate rigorously where the candidates *cannot* be global minimizers.

Our approach is as follows: we discretize the $(\bar{\psi}, \beta)$ parameter space to some desired accuracy and for each point, we test the four ansatz and several other candidates obtained from random initial coefficients. When one of the four ansatz has verified lower energy than the others, up to translational symmetries, we label that point accordingly and otherwise leave the point blank. Figure 2(a) shows the resulting diagram for small parameter values with $(N_x, N_y) = (4, 2), \nu = 1.01, M = 20$. At each point, 30 trials of the Newton iteration were tried and verified rigorously. Note that the points below $\beta = \bar{\psi}^2$ could have been skipped since the constant state is known to be the global minimizer in that regime [14]. This diagram matches the one obtained in the supplementary materials with linear stability analysis.

Figure 2(b) shows the phase diagram near $(\bar{\psi}, \beta) = (0.5, 0.6)$ where localized patterns have been observed. The domain is the same size but $M = 30$ to accommodate the larger β. At each point, 15 trials were tried and verified, leading to points that have lower energy than the atoms or constant states. This indeed shows the existence of a region where localized patterns are more energetically favourable. This region gives an estimate of the full coexistence region that ultimately cannot be made explicit without more refined techniques.

4.6. Rigorous results for two-mode PFC

As a final example, table 5 shows three verified steady states for two-mode PFC with $q = 1/\sqrt{2}$, $(\bar{\psi}, \beta) = (0.09, 0.025)$, $(N_x, N_y) = (12, 4)$, $\nu = 1.01$ and $M = 64$. Note that here, $L_x = 2\sqrt{2}\pi N_x$ and $L_y = 2\sqrt{2}\pi L_y$ to fit the symmetry of the square lattice. The second state shows two grains slipping on each other; in contrast, especially to the result for hexagonal lattices, the third state is a grain boundary with *non-zero* misorientation. Here, the rectangular domains with Neumann boundary conditions can support the geometry of the square lattice at 0° *and* 45° rotations, so we can observe their coexistence. Since this result can be extended to larger domains by simple tiling operations, we conclude that straight grain boundaries *can* be steady states even in infinite domains where boundary conditions cannot 'help' stabilizing such defects.

Table 5. Data on steady states for $(\bar{\psi}, \beta) = (0.09, 0.025)$ and $(N_x, N_y) = (12, 4)$ in the two-mode PFC model with $q = 1/\sqrt{2}$. E_0 is the energy of the constant state for two-mode PFC. $E[\bar{a}]$ is listed for comparison purposes but it is not rigorously bounded.

Visualization	r_* r^*	$E[\bar{a}] - E_0$	Morse index
	2.0×10^{-12} 3.6×10^{-4}	-2.758×10^{-5}	0
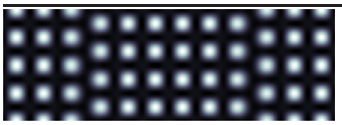	6.5×10^{-12} 1.3×10^{-4}	-2.319×10^{-5}	0
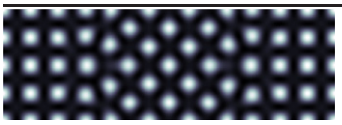	2.4×10^{-11} 4.2×10^{-5}	-2.244×10^{-5}	0

Moreover, this grain boundary was observed to be (numerically) stable in two-mode PFC simulations in the sense that small random perturbations of the phase field always converged back to the grain boundary state. This is not a rigorous proof of stability in H^2, but it gives a good indication that grain boundaries are likely to be stable features in the PFC model.

5. Connections between steady states

Suppose Ψ_1, Ψ_2 represent two steady states, we say that there is a connection (or a connecting orbit) from Ψ_1 to Ψ_2 if there exists a solution $\psi(t)$ with the property that

$$\lim_{t\to-\infty} \psi(t) = \Psi_1 \quad \text{and} \quad \lim_{t\to+\infty} \psi(t) = \Psi_2.$$

More precisely, the connecting orbit leaves the unstable manifold of Ψ_1 and ends up in the stable manifold of Ψ_2. Since the PFC equation is a gradient flow, there cannot exist non-trivial homoclinic connections so there is a natural *hierarchy* of steady states expressed through heteroclinic connections. This concept is extremely useful to 'visualize' the energy landscape.

States with Morse index 0 are stable (for fixed parameters) and are thus at the bottom of the hierarchy. Those states with Morse index 1 have one unstable direction, so there are two distinct perturbations that lead away from the state. For states with Morse index 2, two unstable directions span infinitely many such perturbations, and so on. To detect connections, we propose to initialize a PFC flow near an unstable steady state offset by such perturbations. If the flow becomes close enough to another known steady states, we stop and propose a *conjectured* connection between the two steady states. This procedure often allows us to find unknown steady states: when the flow stagnates, the Newton iteration can be run and often converges in very few steps to a steady state that can be verified. Alternatively, we could check for inclusion in the target r^* ball, but this is a very restrictive criterion that limits our numerical investigation, especially when obtaining connections to unstable states. We use the PFC scheme detailed in [44].

While we cannot for the moment prove such claims because 'parameterizing' the infinite dimensional stable manifold of the unstable steady states is highly non-trivial, we are aware of

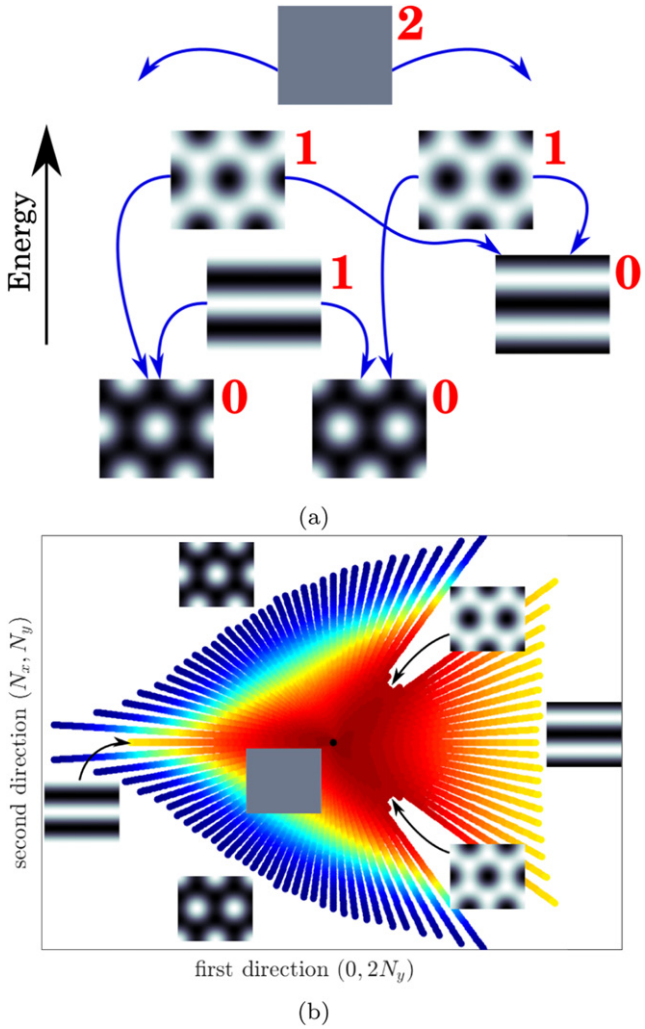

Figure 3. Connection diagram (a) where arrows represent likely connections; the constant state is connected to all others. The vertical axis gives the ordering in energy while the numbers give the Morse index. (b) Energy visualization with respect to the unstable directions of the constant state. This diagram illustrates how the unstable directions combine to transform the constant state into other lower energy states. The unstable directions serve as the main axes and the lines represent different initial perturbations. The length of the lines indicate the number of PFC steps before the flows becomes close to the connecting steady states. Colours represent energy (red for high and blue for low energy).

some preliminary work in this direction [47]. That said, computer-assisted proofs of connecting orbits from saddle points to asymptotically stable steady states in parabolic PDEs are starting to appear [48, 49].

We first consider the standard parameters $(\bar{\psi}, \beta) = (0.07, 0.025)$ and use the very small domain $(N_x, N_y) = (2, 1)$. This choice is made to ensure that the constant state has Morse index 2 in X to simplify the visualization. We find seven steady states: both possible translations of the atoms, stripes and donuts state, and the trivial constant state. Following the program

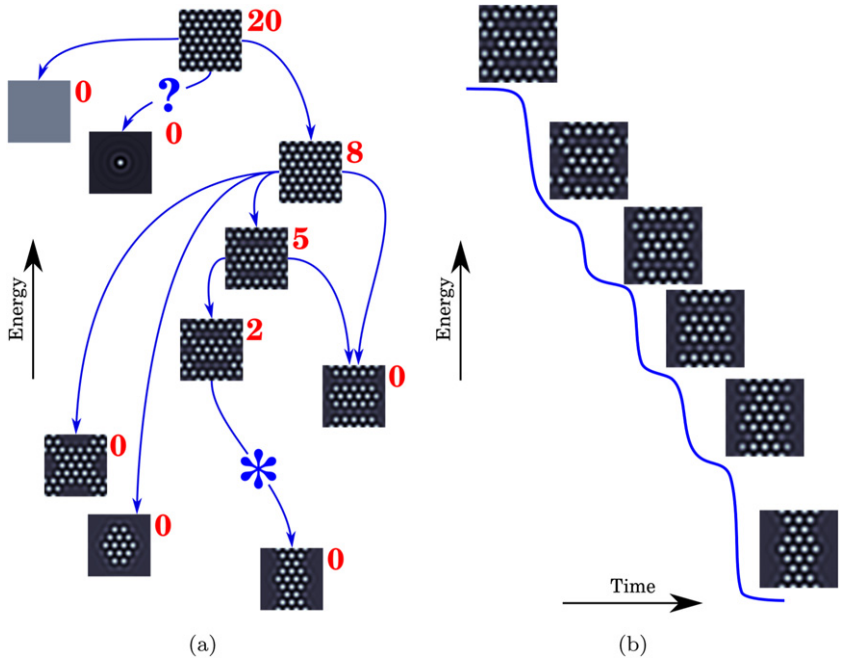

Figure 4. Connection diagram (a) where arrows represent a few of the connections found. The two hexagonal lattice states differ in their amplitude and stability. The vertical axis roughly indicates the energy while the numbers give the Morse indices. We could not obtain (nor disprove) a connection to the single atom state, indicated with the question mark. The connection labelled with a star is broken down in the energy plot to the right (b). These states appear to be metastable intermediates where the energy gradient becomes small and the evolution slows down considerably. The blue curve shows the energy as a function of time in arbitrary units, highlighting momentaneous 'flats' in the evolution.

described above, we can construct the 'connection diagram' shown in figure 3(a) with the arrows indicating that a connection was found from a state to the other. Note in particular that the stable stripes state to the right *numerically* decays into the appropriately shifted hexagonal lattices, but this is a slow process as the sine modes must grow out of numerical noise. This clearly shows that our method cannot be used to guarantee stability in H^2 because it *cannot* depend on translational shifts.

We also propose a visualization method for such diagrams shown in figure 3(b). Take for example the constant state with its two unstable directions given by the coefficients $a_{0,2N_y}$ and a_{N_x,N_y}. We place the constant state at the origin and plot radial lines along linear combination of the unstable directions. The line length corresponds to the number of PFC steps needed to approach the target steady states. In addition, we can colour the points along the line as a function of energy to indicate energetic relationships. A variant would be to show the energy as the z-component of a surface; essentially giving an indirect visualization of the energy landscape through 2D unstable manifolds. In particular, this diagram clarifies the relationships between the steady states. For instance, the stripes states are formed by adding the $a_{0,2N_y}$ mode to the constant state while the donuts are combinations of the atoms and stripes states.

We now consider the localized patterns regime to illustrate these ideas with states of high Morse index. We do not attempt to build a higher dimensional visualization, but simply attempt

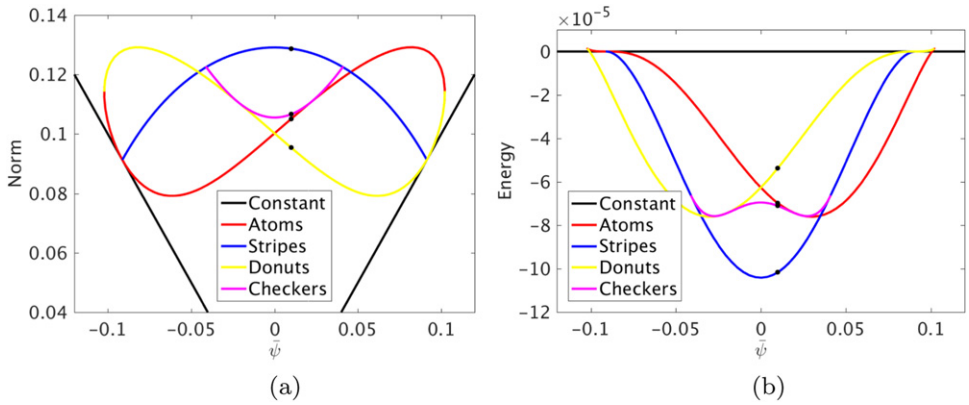

Figure 5. Continuation (bifurcation) diagram showing the L^2 norm of the phase (a) and the energy offset by E_0 (b) as functions of $\bar{\psi}$. The dots represent the starting points at $(\bar{\psi}, \beta) = (0.01, 0.025)$.

to recover the 'pathways' between the highly unstable hexagonal lattice with Morse index 20 towards stable steady states. This is visualized in the connection diagram of figure 4(a) which includes a few states of table 3. In (b), we plot the energy along the PFC flow starting from the index 2 state; this plot can be thought of as one of the rays in a diagram like figure 3(b). Note that along the flow, the energy decreases in 'steps' corresponding to changes in topology, i.e. the formation (or removal) of atoms. In this process, we could not verify that these intermediates are steady states since the Newton iteration always converged to the endpoint; we then suppose they are short-lived 'metastable' states.

It is difficult to obtain perturbations that can flow to *desired* steady states, especially when they are unstable; see how only a few directions reach the Morse index 1 states in figure 3(b). Indeed, unless 'trivial' combinations of the unstable direction happen to go to an unstable state, we are unlikely to find such connections numerically. Similarly, our attempts to find a perturbation that connects the starting lattice to the single atom state were unfruitful.

6. Parameter continuation for steady states

A verified steady state $\widetilde{a}$ for some parameter $(\bar{\psi}, \beta)$ is usually part of a family of steady states representing a 'phase' of matter. In fact, the candidate minimizers defined in supplementary material section 1 as functions of $(\bar{\psi}, \beta)$ approximate such families, or branches in the *bifurcation diagram*. In this context, we can construct such branches by starting at a known steady state, vary $\bar{\psi}$ and find the closest steady state at this new parameter value.

Several verified techniques exist for following branches, see [39, 50] for an application to Ohta–Kawasaki. We use non-verified pseudo-arclength continuation [51] in $\bar{\psi}$. Note that the unstable direction that is to followed is precisely given by the one corresponding to the 'fixed' $a_{0,0} = \bar{\psi}$ condition and this is one of the reasons that we chose to enforce this directly in the formulation of F. As a possible extension, 2D manifolds can be constructed in two-parameter continuation when both parameters are allowed to vary, see [52].

Figure 5 shows the norm (a) and offset energy (b) of the main ansatz at $(\bar{\psi}, \beta) = (0.07, 0.025)$ are plotted as functions of $\bar{\psi}$. The domain is kept small with $(N_x, N_y) = (2, 1)$ to keep the bifurcation diagram as simple as possible. The atoms and donuts branches are actually the same since we can continue the branches through the folds at $\bar{\psi} = \pm\sqrt{5/12\beta}$. This branch

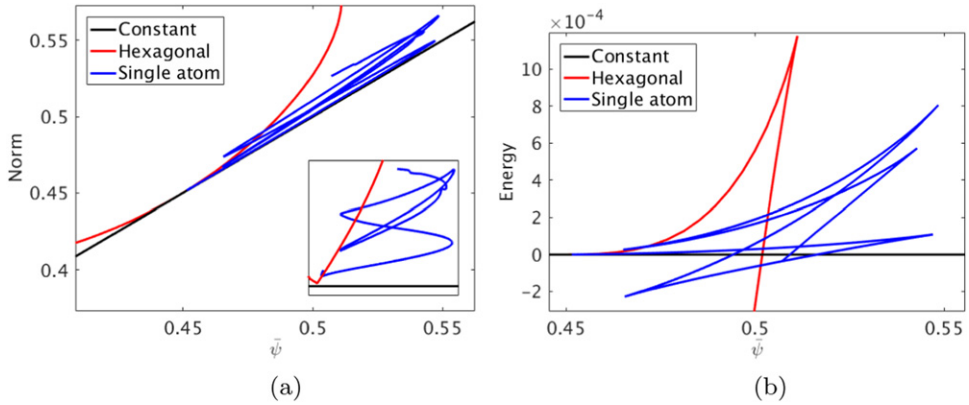

Figure 6. Continuation (bifurcation) diagram showing the L^2 norm of the phase (a) and the energy offset by E_0 (b) as functions of $\bar{\psi}$. The inset in (a) shows the norm of $\psi - \bar{\psi}$ to better illustrate the snaking phenomenon. Both the hexagonal and single atom branches appear to loop on themselves.

intersects the checkers state at $\beta = 15\bar{\psi}^2$ and the constant and stripes states at $\beta = 3\bar{\psi}^2$. The energy plot (b) clearly shows that the donuts state is the 'proper' hexagonal lattice for $\bar{\psi} < 0$. We note that varying β simply causes the branches to dilate. For example, we expect the 2D hexagonal steady states manifold to be a 'conic' figure-eight.

Other 'new' branches will appear for larger domains or higher β. In particular, figure 6 shows the atoms/donuts branch and the single atom branch in the localized patterns regime near $(\bar{\psi}, \beta) = (0.5, 0.6)$ with $(N_x, N_y) = (7, 4)$. Again, (a) shows the L^2 norm and (b) shows the energy of the phase field as functions of $\bar{\psi}$. The hexagonal lattice traces out its usual figure-eight pattern while the single atom (and other localized states in general) traces out a complicated looping path. Such branches illustrate the 'snaking' phenomenon previously observed in modified Swift–Hohenberg equations that support such localized patterns, see [45] for example. We observe that the path loops on itself in one direction as the single atom evolves into a localized pattern with 9, 7 then 4 atoms before looping back with a 90° rotation. In the other direction, the branch moves towards the transition between the hexagonal and constant states where it again loops back. This computation is difficult because the truncation must remain large and the pseudo-arclength step size must remain small; if the step size is larger than 0.0005, the branch breaks away towards the hexagonal lattice solution.

7. Conclusion

We surveyed the basic properties of the PFC equation as a dynamical system in the framework of rigorous numerics. Thanks to an application of the radii polynomial approach, we were able to verify the existence of steady states close to numerically computed approximations. This provided us with important *verified* information regarding the behaviour of the energy landscape, especially in terms of energetic relationships between steady states. We were also able to provide partial stability results with the caveat that they only applied to the cosine Fourier series. The Morse indices given were lower bounds in H^2—thus those steady states with Morse index higher than 0 must be unstable in H^2.

Such ideas were applied in various regimes of the PFC equation to verify that certain important patterns are steady states (as opposed to metastable intermediates) including single atoms,

other localized patterns and grain boundaries. In particular, we showed that two-mode PFC supports a non-zero misorientation grain boundary *steady state* that we expect to be stable. We also showed the construction of the phase diagram with our fully nonlinear approach.

Finally, we used such results to further investigate the energy landscape through connections or orbits and through parameter continuation. Connections reveal the energetic and dynamical relationships between steady states, highlighting the behaviour of unstable patterns as they reach states with lower energy. Continuation is especially useful to understand how the important states evolve across parameter space, highlighting the surprising behaviour of the hexagonal lattice patterns and the snaking behaviour of localized patterns.

Our work suggests several interesting directions for future work. On one hand, our connection results could be made rigorous with a technique to prove orbits from unstable to stable manifolds. This is a complicated problem because the stable manifold is infinite dimensional and special techniques must be applied to properly parameterize its 'dominant' submanifold. On the other, our continuation results could also be made rigorous or extended to two-parameter continuation to reveal more interesting behaviour. Alternatively, parameter continuation could be applied to the domain size, for example to investigate problems in elasticity.

Acknowledgment

RC and JPL were supported by an NSERC (Canada) through their Discovery Grants Program. JPL also acknowledges support from an NSERC Accelerator Award.

ORCID iDs

Gabriel Martine-La Boissonière https://orcid.org/0000-0001-8848-8984
Rustum Choksi https://orcid.org/0000-0003-2419-9520

References

[1] Elder K R, Katakowski M, Haataja M and Grant M 2002 Modeling elasticity in crystal growth *Phys. Rev. Lett.* **88** 245701
[2] Swift J and Hohenberg P C 1977 Hydrodynamic fluctuations at the convective instability *Phys. Rev.* A **15** 319–28
[3] Martine La Boissonière G and Choksi R 2018 Atom based grain extraction and measurement of geometric properties *Modelling Simul. Mater. Sci. Eng.* **26** 035001
[4] Martine La Boissonière G, Choksi R, Barmak K and Esedoḡlu S 2019 Statistics of grain growth: experiment versus the phase-field-crystal and Mullins models *Materialia* **6** 100280
[5] Backofen R, Barmak K, Elder K E and Voigt A 2014 Capturing the complex physics behind universal grain size distributions in thin metallic films *Acta Mater.* **64** 72–7
[6] Emmerich H, Löwen H, Wittkowski R, Gruhn T, Tóth G I, Tegze G and Gránásy L 2012 Phase-field-crystal models for condensed matter dynamics on atomic length and diffusive time scales: an overview *Adv. Phys.* **61** 665–743
[7] Archer A J, Ratliff D J, Rucklidge A M and Subramanian P 2019 Deriving phase field crystal theory from dynamical density functional theory: consequences of the approximations *Phys. Rev.* E **100** 022140
[8] Greenwood M, Ofori-Opoku N, Rottler J and Provatas N 2011 Modeling structural transformations in binary alloys with phase field crystals *Phys. Rev.* B **84** 064104
[9] Seymour M and Provatas N 2016 Structural phase field crystal approach for modeling graphene and other two-dimensional structures *Phys. Rev.* B **93** 035447
[10] Hirvonen P *et al* 2016 Multiscale modeling of polycrystalline graphene: a comparison of structure and defect energies of realistic samples from phase field crystal models *Phys. Rev.* B **94** 035414

[11] Archer A J, Rucklidge A M and Knobloch E 2015 Soft-core particles freezing to form a quasicrystal and a crystal-liquid phase *Phys. Rev.* E **92** 012324
[12] Subramanian P, Archer A J, Knobloch E and Rucklidge A M 2016 Three-dimensional icosahedral phase field quasicrystal *Phys. Rev. Lett.* **117** 075501
[13] Subramanian P, Archer A, Knobloch E and Rucklidge A 2018 Spatially localized quasicrystalline structures *New J. Phys.* **20** 11
[14] Shirokoff D, Choksi R and Nave J-C 2015 Sufficient conditions for global minimality of metastable states in a class of non-convex functionals: a simple approach via quadratic lower bounds *J. Nonlinear Sci.* **25** 539–82
[15] Koch H, Schenkel A and Wittwer P 1996 Computer-assisted proofs in analysis and programming in logic: a case study *SIAM Rev.* **38** 565–604
[16] Nakao M T 2001 Numerical verification methods for solutions of ordinary and partial differential equations *Numer. Funct. Anal. Optim.* **22** 321–56
[17] Tucker W 2011 *Validated Numerics: A Short Introduction to Rigorous Computations* (Princeton, NJ: Princeton University Press)
[18] van den Berg J B and Lessard J P 2015 Rigorous numerics in dynamics *Not. AMS* **62** 1057–61
[19] Gómez-Serrano J 2019 Computer-assisted proofs in PDE: a survey *SeMA J.* **76** 459–84
[20] Wu K A, Adland A and Karma A 2010 Phase-field-crystal model for FCC ordering *Phys. Rev.* E **81** 061601
[21] Lanford III O E III 1982 A computer-assisted proof of the Feigenbaum conjectures *Bull. Am. Math. Soc.* **6** 427–35
[22] Tucker W 2002 A rigorous ODE Solver and Smale's 14th problem *Found. Comput. Math.* **2** 53–117
[23] Plum M 1992 Explicit H_2-estimates and pointwise bounds for solutions of second-order elliptic boundary value problems *J. Math. Anal. Appl.* **165** 36–61
[24] Zgliczyński P 2004 Rigorous numerics for dissipative partial differential equations. II. Periodic orbit for the Kuramoto–Sivashinsky PDE—a computer-assisted proof *Found. Comput. Math.* **4** 157–85
[25] Zgliczyński P and Mischaikow K 2001 Rigorous numerics for partial differential equations: the Kuramoto–Sivashinsky equation *Found. Comput. Math.* **1** 255–88
[26] Nakao M T, Hashimoto K and Watanabe Y 2005 A numerical method to verify the invertibility of linear elliptic operators with applications to nonlinear problems *Computing* **75** 1–14
[27] Breuer B, McKenna P J and Plum M 2003 Multiple solutions for a semilinear boundary value problem: a computational multiplicity proof *J. Differ. Equ.* **195** 243–69
[28] Day S, Hiraoka Y, Mischaikow K and Ogawa T 2005 Rigorous numerics for global dynamics: a study of the Swift–Hohenberg equation *SIAM J. Appl. Dyn. Syst.* **4** 1–31
[29] Maier-Paape S, Mischaikow K and Wanner T 2007 Structure of the attractor of the Cahn–Hilliard equation on a square *Int. J. Bifur. Chaos Appl. Sci. Eng.* **17** 1221–63
[30] Nakao M T, Plum M and Watanabe Y 2019 *Numerical Verification Methods and Computer-Assisted Proofs for Partial Differential Equations* (*Springer Series in Computational Mathematics*) vol 53 (Singapore: Springer)
[31] Arioli G and Koch H 2010 Computer-assisted methods for the study of stationary solutions in dissipative systems, applied to the Kuramoto–Sivashinski equation *Arch. Ration. Mech. Anal.* **197** 1033–51
[32] Arioli G, Koch H and Terracini S 2005 Two novel methods and multi-mode periodic solutions for the Fermi–Pasta–Ulam model *Commun. Math. Phys.* **255** 1–19
[33] Yamamoto N 1998 A numerical verification method for solutions of boundary value problems with local uniqueness by Banach's fixed-point theorem *SIAM J. Numer. Anal.* **35** 2004–13
[34] Galias Z and Zgliczyński P 2007 Infinite-dimensional Krawczyk operator for finding periodic orbits of discrete dynamical systems *Int. J. Bifur. Chaos* **17** 4261–72
[35] Plum M 2009 Computer-assisted proofs for semilinear elliptic boundary value problems *Japan. J. Ind. Appl. Math.* **26** 419–42
[36] Day S, Lessard J-P and Mischaikow K 2007 Validated continuation for equilibria of PDEs *SIAM J. Numer. Anal.* **45** 1398–424
[37] Arioli G and Koch H 2010 Integration of dissipative partial differential equations: a case study *SIAM J. Appl. Dyn. Syst.* **9** 1119–33

[38] van den Berg J B and Lessard J-P 2018 Introduction to rigorous numerics in dynamics: general functional analytic setup and an example that forces chaos *Rigorous Numerics in Dynamics* (*Proceedings of Symposia in Applied Mathematics*) vol 74 (Providence, RI: American Mathematical Society) pp 1–25
[39] van den Berg J B and Williams J F 2017 Validation of the bifurcation diagram in the 2D Ohta–Kawasaki problem *Nonlinearity* **30** 1584
[40] van den Berg J B and Williams J F 2019 Rigorously computing symmetric stationary states of the Ohta–Kawasaki problem in three dimensions *SIAM J. Math. Anal.* **51** 131–58
[41] Moore R E 1966 *Interval Analysis* vol 4 (Englewood Cliffs, NJ: Prentice-Hall)
[42] Rump S M 1999 INTLAB—interval laboratory *Developments in Reliable Computing* (Netherlands: Springer) pp 77–104
[43] Hargreaves G I 2002 Interval analysis in MATLAB *Numerical Algorithms* (United Kingdom: The University of Manchester)
[44] Elsey M and Wirth B 2013 A simple and efficient scheme for phase field crystal simulation *ESAIM: Math. Modelling Numer. Anal.* **47** 1413–32
[45] Lloyd D J B, Sandstede B, Avitabile D and Champneys A R 2008 Localized hexagon patterns of the planar Swift–Hohenberg equation *SIAM J. Appl. Dyn. Syst.* **7** 1049–100
[46] van den Berg J B, Deschênes A, Lessard J-P and Mireles James J D 2015 Stationary coexistence of hexagons and rolls via rigorous computations *SIAM J. Appl. Dyn. Syst.* **14** 942–79
[47] van den Berg J B, Jaquette J and Mireles James J 2021 Validated numerical approximation of stable manifolds for parabolic partial differential equations (arXiv:2004.14830v2)
[48] Cyranka J and Wanner T 2018 Computer-assisted proof of heteroclinic connections in the one-dimensional Ohta–Kawasaki model *SIAM J. Appl. Dyn. Syst.* **17** 694–731
[49] Reinhardt C and Mireles James J D 2019 Fourier–Taylor parameterization of unstable manifolds for parabolic partial differential equations: formalism, implementation and rigorous validation *Ind. Math.* **30** 39–80
[50] van den Berg J B, Lessard J-P and Mischaikow K 2010 Global smooth solution curves using rigorous branch following *Math. Comput.* **79** 1565–84
[51] Keller H B 1987 *Lectures on Numerical Methods in Bifurcation Problems* (*Tata Institute of Fundamental Research Lectures on Mathematics and Physics*) vol 79 (Berlin: Springer) Published for the Tata Institute of Fundamental Research, Bombay
[52] Gameiro M, Lessard J-P and Pugliese A 2016 Computation of smooth manifolds via rigorous multi-parameter continuation in infinite dimensions *Found. Comput. Math.* **16** 531–75